Soils and Foundations 2012;52(1):18–37

The Japanese Geotechnical Society

Soils and Foundations

www.sciencedirect.com
journal homepage: www.elsevier.com/locate/sandf

Long-term consolidation analysis of a large-scale embankment construction on soft clay deposits using an elasto-viscoplastic model

Mojtaba Mirjalili[a], Sayuri Kimoto[a], Fusao Oka[a,*], Tatsuo Hattori[b]

[a]*Department of Civil and Earth Resources Engineering, Kyoto University, Kyotodaikagu-katsura C1-4, Nishikyo-ku, Kyoto 615-8540, Japan*
[b]*Kinki Regional Development Bureau, MLIT, Osaka, Japan*

Available online 7 February 2012

Abstract

In this paper, the consolidation analysis of a large-scale embankment construction in Osaka City is presented, where a conventional levee with a height of about 8 m has been extended to a super levee with a total width of 215 m. The ground consists of alluvial sandy layers and soft clay deposits, which have been locally improved by several methods, including deep mixing beneath the conventional levee and the combination of sand drains and sand compaction piles under the extended back slope. A long-term consolidation analysis of this super levee construction is carried out using an elasto-viscoplastic constitutive model. The layered construction procedure is applied to properly simulate the construction sequence of the super levee. The effects of the structural degradation and the strain dependency of the shear modulus, as two aspects of destructuration in clay materials, are studied in terms of the consolidation behavior for the unimproved case. For the improved case, the analysis is implemented by including the ground-improved zones in the finite element simulation. The field observation data obtained during the preloading process, before the construction of the super levee, are employed to verify the assumptions and to calibrate the material properties of the improved layers. The effects of destructuration in the natural ground cases are observed as excess pore pressure build-up after construction and strain localization. The effects of ground improvement techniques are studied through a comparison of the deformation results and the excess pore water pressure responses with the natural ground cases. The numerical results show that it is important to carefully estimate the unequal long-term settlement for the construction of large-scale embankments.

Keywords: Super levee; Soft clay; Consolidation; Elasto-viscoplastic model; Creep; Ground improvement; Finite element method (**IGC:** E2)

1. Introduction

Flooding and sediment-related disasters have been the main causes of damage all around the world. The investigation of past flood disasters has raised serious concerns regarding the vulnerability of levees and flood-control structures. Considering the low reliability and the weakness of conventional river embankments against disasters, a high-standard embankment, a so-called 'super levee', was firstly proposed in Japan as protection along major rivers where absolutely no embankment collapse can be allowed (Kundzewicz and Takeuchi, 1999). A super levee is constructed by widening the back slope of a normal river embankment to a broad width (200–500 m) with a gentle slope on which urban buildings and traffic facilities are developed. The super levees can withstand even over-flow, so that destruction by an embankment break and the resultant flooding can be prevented. In addition, a super levee is expected to have more resistibility against earth-quakes and the consequent damage they cause.

*Corresponding author.
E-mail address: oka.fusao.2s@kyoto-u.ac.jp (F. Oka).

Peer review under responsibility of The Japanese Geotechnical Society
doi:10.1016/j.sandf.2012.01.010

In the past few years, many parts of the continuous levee line in the downstream of the Yodo River in Osaka City, Japan, have been widened to super levees. The Yodo River is the principal river in the Osaka metropolitan region and has a high risk of flooding. Any levee breakage alongside this river would result in severe damage and human fatalities. Despite the advantages of super levees, in comparison to normal levees, several issues prevail concerning the construction of such massive embankments, particularly on soft ground deposits beside rivers. On the other hand, the necessity of super levee construction in that area, as part of the flood control management system, demands a comprehensive study on the failure mechanism and the overall behavior of embankments over soft clay strata.

In the present study, the consolidation analysis of a super levee construction along the Yodo River at Torishima is examined. Almost 10 years after the completion of the Torishima super levee, subsidence and superficial cracks were observed around the road pavement on top of the super levee (Oka, 2009). Subsequently, a comprehensive investigation was conducted to find the causes of the deformations in this case. The outcome of the investigation could then be employed to revise the current construction guidelines for super levees.

The ground layers at the Torishima super levee site consist of alluvial sandy layers and soft clay layers, which were locally improved before the construction of the levee. The elasto-viscoplastic constitutive model proposed by Kimoto and Oka (2005) is adopted to simulate the behavior of the clay layers in the two-dimensional finite element consolidation analysis. The embankments of the super levee are properly modeled by finite element mesh so that the stiffness and the consolidation of the embankments can be considered in addition to embankment loading.

The consolidation analysis is divided into two phases. The first phase is the consolidation analysis of the natural (unimproved) ground, for which the characteristic behavior of the clay layers in particular is studied by considering the effects of destructuration aspects, namely, the structural degradation and the strain dependency of the elastic shear modulus, on the long-term consolidation response. Destructuration is usually used to describe the progressive damage to the interparticle bonds during plastic straining; this is referred to as sensitivity in natural soft clay. The sensitivity of clay is defined as the ratio of the clay's undisturbed strength to its remolded strength (Terzaghi, 1944). This sensitivity may range from about 4 to values of over 100. For the soft clay found in the Osaka area, sensitivity values of 4–10 are quite common. This indicates the high sensitivity of this type of clay, although larger values have been reported in some areas (e.g., Adachi et al., 1995; KG-NET, 2007). Certain types of unstable behavior, caused by the destructuration of sensitive clay, such as the anomalous pore water pressure response after the completion of loading and secondary creep, have been reported by many researchers, e.g., Mesri and Choi (1979), Mitchell (1986), and Lavallée et al. (1992). Structural degradation can be described with an elasto-viscoplastic constitutive model using material parameters β and σ'_{maf}. This has been contributed by Kimoto and Oka (2005).

The second phase is the consolidation analysis of the improved ground case. The ground settlement data existing during the preloading procedure, before construction of the super levee, are used to verify the assumptions and to calibrate the material parameters of the improved layers. The results of each phase, such as deformations and excess pore water pressure responses, are presented and discussed. Comparisons are made through the deformations and the excess pore pressure results for each phase, to evaluate the consolidation mechanism and the effect of ground-improvement techniques.

2. Site description and project history

The Torishima super levee is located on the left bank of the Yodo River, which flows into Osaka Bay, in the western part of Osaka City. The super levee extends about 450 m in length along the riverbank. Due to the 1995 Kobe (Great Hanshin) Earthquake, about 2000 m of the continuous levee line along the Yodo River, including the Torishima dike, was severely damaged by the liquefaction of the foundation soil (Matsuo, 1996). Thereafter, the rebuilding of the levee on that site was initiated by the construction of a super levee. The main levee, with a height of 8.1 m, was built on a foundation improved by deep mixing. The back slope extension was constructed on a foundation improved by sand drains and sand compaction piles, with a gentle slope of approximately $1V{:}29H$. Prior to the construction of the super levee, the preloading process had been conducted to improve the characteristics of the clay layers by pre-consolidation.

The cross section of the super levee, the subsurface layers, and the ground-improvement details are schematically presented in Fig. 1. The general stratigraphic profile of the Torishima area is composed of alluvial sandy layers and soft clay layers overlying a dense gravelly layer, and subsequently, a rather stiff clay layer at a depth of about 35 m. Em1 and Em2 represent the embankment fill materials of the main levee and of the extended back slope, respectively. B1 represents the topsoil material with a thickness of about 2.25 m. As2 is the upper alluvial sand layer, which has a thickness of approximately 8.5 m, Ac2 is the alluvial soft clay layer, which has a thickness of 12 m, As1 is the lower alluvial sand layer, which has a thickness of 5.5 m, and Ac1 is the alluvial clay deposit. Dg and Dc indicate the diluvium sandy gravel and the rather stiff clay deposits, respectively. As shown in Fig. 1, deep mixing (DM) was performed up to 10 and 14 m in depth beneath the main levee to improve the whole thickness of layers B1 and As2, respectively, and to slightly improve the upper part of layer Ac2. Deep mixing was performed as DM

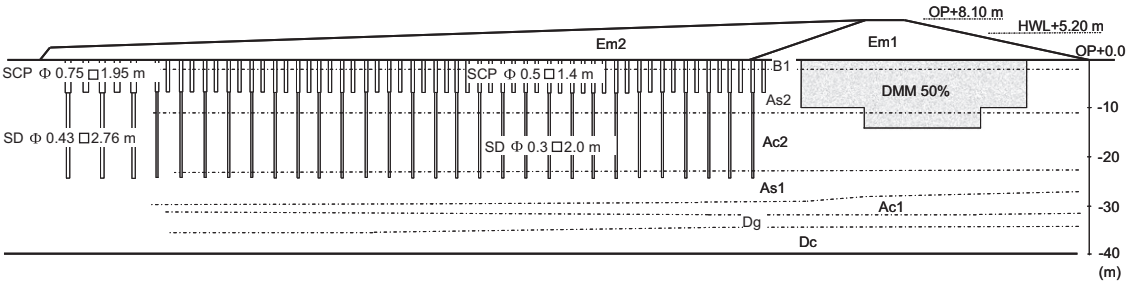

Fig. 1. Cross section of the Torishima super levee, soil profile, and ground-improvement techniques.

walls with a thickness of 1.6 m in a grid pattern of 5.8 m × 4.8 m, which provided an average improvement ratio of 50% in the DM-improved area. The vertical sand drains were installed up to a depth of about 24.0 m beneath the back slope extension in different diameters and patterns according to the design requirements. At the upper part of the sand drains, sand compaction piles (SCP) were positioned to a depth of 6.7 m, covering the entire depth of layer B1 and half the depth of layer As2, mostly to prevent the liquefaction failure of these layers. The SCPs were arranged in smaller square patterns within SD grids, of which the SCPs were alternately installed over the sand drains.

3. Development of the numerical model

In order to study the long-term consolidation behavior of the super levee construction on the soft clay strata, two-dimensional numerical analyses are developed under fully water-saturated conditions. The behavior of the clay layers is simulated using an elasto-viscoplastic model, while the elastic behavior is applied for the sand and the gravel layers.

3.1. Elasto-viscoplastic constitutive model

As mentioned earlier, an elasto-viscoplastic constitutive model, proposed by Kimoto and Oka (2005) is adopted for the numerical simulation of the clayey materials. The model is an extension of the rate-dependent model for water-saturated clay, firstly proposed by Adachi and Oka (1982), which combines the Cam-clay model (Roscoe et al., 1963) and Perzyna's (1963) overstress type of viscoplasticity for the elasto-viscoplastic formulation. Kimoto and Oka (2005) improved the original model by Adachi and Oka (1982) in order to overcome the structural degradation of the soil skeleton, considering the shrinkage of both the overconsolidated boundary surface and the static yield surface with respect to the accumulation of viscoplastic strain. In this section, the features of the model are described as can be found in Kimoto and Oka (2005). However, the model is modified here in two ways, namely, the variation in the stress ratio at failure by Lode's angle and the introduction of a new definition for the dilatancy coefficient.

In the adopted constitutive model, Terzaghi's effective stress for water-saturated soil is used as

$$\sigma_{ij} = \sigma'_{ij} + U_w \delta_{ij} \tag{1}$$

where σ_{ij} is the total stress tensor, σ'_{ij} is the effective stress tensor, U_w is the pore water pressure, and δ_{ij} is Kronecker's delta. In addition, total strain rate tensor $\dot{\varepsilon}_{ij}$ is assumed to be divided into two parts, namely

$$\dot{\varepsilon}_{ij} = \dot{\varepsilon}^e_{ij} + \dot{\varepsilon}^{vp}_{ij} \tag{2}$$

where $\dot{\varepsilon}^e_{ij}$ denotes the elastic strain rate tensor and $\dot{\varepsilon}^{vp}_{ij}$ is the viscoplastic strain rate tensor. The elastic strain rate tensor can be expressed as

$$\dot{\varepsilon}^e_{ij} = \frac{1}{2G}\dot{S}_{ij} + \frac{\kappa}{3(1+e)}\frac{\dot{\sigma}'_m}{\sigma'_m}\delta_{ij} \tag{3}$$

in which G is the elastic shear modulus, S_{ij} is the deviatoric stress tensor ($S_{ij} = \sigma'_{ij} - \sigma'_m \delta_{ij}$), σ'_m is the mean effective stress, and the superimposed dot denotes the time differentiation. κ is the swelling index and e_0 is the initial void ratio. The modification of elastic shear modulus G will be presented in the next section.

An overconsolidation boundary surface is assumed to delineate the normally consolidated (NC) region and the overconsolidated (OC) region as

$$f_b = \overline{\eta}^*_{(0)} + M^*_m \ln(\sigma'_m/\sigma'_{mb}) = 0 \tag{4}$$

where $f_b < 0$ indicates the overconsolidated region and $f_b \geq 0$ shows the normally consolidated region. $\overline{\eta}^*_{(0)}$ is the relative stress ratio defined by

$$\overline{\eta}^*_{(0)} = \sqrt{(\eta^*_{ij} - \eta^*_{ij(0)})(\eta^*_{ij} - \eta^*_{ij(0)})} \tag{5}$$

in which subscript (0) denotes the initial state before deformation and η^*_{ij} is the stress ratio tensor. σ'_{mb} controls the size of the OC boundary surface. M^*_m is the value of $\eta^* = \sqrt{\eta^*_{ij}\eta^*_{ij}}$ when the volumetric strain increment changes from compression to swelling. In order to include Mohr–Coulomb's failure criterion with zero cohesion, stress ratio M^*_m is considered to be a function of Lode's angle θ given by

$$\theta = \frac{1}{3}\cos^{-1}\left[\frac{3\sqrt{3}}{2}\frac{J_3}{J_2^{3/2}}\right] \tag{6}$$

$$M_m^*(\theta)=\frac{6\sqrt{2}\sin\phi}{(3+3\sin\phi)\sin\theta+\sqrt{3}(3-\sin\phi)\cos\theta} \tag{7}$$

where J_2 and J_3 are the second and the third invariants of the deviatoric stress tensor, respectively, and ϕ is the internal frictional angle. Lode's angle varies in the range of $0\le\theta\le(\pi/3)$, where $\theta=0$ represents the triaxial compression mode and the maximum value shows the extension mode of loading under triaxial conditions. In Eq. (7), by taking $\theta=0$, the stress ratio at triaxial compression M_{mc}^* can be obtained as

$$M_{mc}^*=\sqrt{\frac{2}{3}}\frac{6\sin\phi}{3-\sin\phi} \tag{8}$$

To describe the structural degradation of clay, strain softening with the accumulated viscoplastic strain is introduced in addition to strain hardening with the viscoplastic volumetric strain as

$$\sigma'_{mb}=\sigma'_{ma}\exp\left(\frac{1+e_0}{\lambda-\kappa}\varepsilon_v^{vp}\right) \tag{9}$$

where σ'_{ma} is assumed to decrease with an increase in viscoplastic strain with

$$\sigma'_{ma}=\sigma'_{maf}+(\sigma'_{mai}-\sigma'_{maf})\exp(-\beta z^h) \tag{10}$$

in which z is the accumulation of the second invariant of the viscoplastic strain rate given by

$$z=\int_0^t \dot{z}dt;\quad \dot{z}=\sqrt{\dot{\varepsilon}_{ij}^{vp}\dot{\varepsilon}_{ij}^{vp}} \tag{11}$$

In Eq. (10), σ'_{mai} and σ'_{maf} are the initial and the final values for σ'_{ma}, respectively. β is a parameter that stands for the changing rate of σ'_{ma}, while the proportion of $n=(\sigma'_{maf}/\sigma'_{mai})$ provides the degree of possible collapse of the soil structure at the initial state. h is an additional degradation parameter with a non-negative value that controls the rate of degradation of the soil skeleton. In this study, the value of this parameter is assumed as $h=1$.

In the following, static yield function f_y has been proposed to explain the mechanical behavior of clay at its static equilibrium state as

$$f_y=\overline{\eta}_{(0)}^*+\tilde{M}^*\ln(\sigma'_m/\sigma'^{(s)}_{my})=0 \tag{12}$$

where $\sigma'^{(s)}_{my}$ denotes the static hardening parameter. Static equilibrium state $f_y=0$ refers to the case when no viscoplastic deformation occurs, which can only be reached after an infinite time.

In the same manner as for the static yield function, viscoplastic potential function f_p is given by

$$f_p=\overline{\eta}_{(0)}^*+\tilde{M}^*\ln(\sigma'_m/\sigma'_{mp})=0 \tag{13}$$

where dilatancy coefficient $\tilde{M}^*$ is defined separately for the overconsolidated region (OC) and the normally consolidated region (NC). In the original definition by Kimoto and Oka (2005), $\tilde{M}^*$ is given by

$$\tilde{M}^*=\begin{cases} M_m^*(\theta) & : \text{NC region}\\ -\dfrac{\sqrt{\eta_{ij}^*\eta_{ij}^*}}{\ln(\sigma'_m/\sigma'_{mc})} & : \text{OC region}\end{cases} \tag{14}$$

in which $\sigma'_{mc}=\sigma'_{mb}$ for the isotropic consolidation. In general, it can be expressed as

$$\sigma'_{mc}=\sigma'_{mb}\exp\left(\frac{\sqrt{\eta_{ij(0)}^*\eta_{ij(0)}^*}}{M_m^*(\theta)}\right) \tag{15}$$

According to the above definition, the value of dilatancy coefficient $\tilde{M}^*$ becomes zero when the stress path coincides with the mean effective stress axis during cyclic loading. Therefore, a new definition for $\tilde{M}^*$ (Kimoto et al., 2007) is introduced here as

$$\tilde{M}^*=\begin{cases} M_m^*(\theta) & : \text{NC region}\\ (\sigma_m^*/\sigma'_{mb})M_m^*(\theta) & : \text{OC region}\end{cases} \tag{16}$$

where σ_m^* denotes the mean effective stress at the intersection of the surface, which has the same shape as f_b, and is given by

$$\sigma_m^*=\sigma'_m\exp\left(\frac{\overline{\eta}_{(0)}^*}{M_m^*(\theta)}\right) \tag{17}$$

The overconsolidation boundary surface, the static yield function, and the viscoplastic potential function are illustrated for isotropically consolidated soil in Fig. 2. σ'_{mb} and $\sigma'^{(s)}_{my}$ change with the structural degradation of the soil skeleton, namely, the viscoplastic strain accumulation. This leads to the gradual shrinkage of the overconsolidation boundary surface, as well as the static yield surface, in

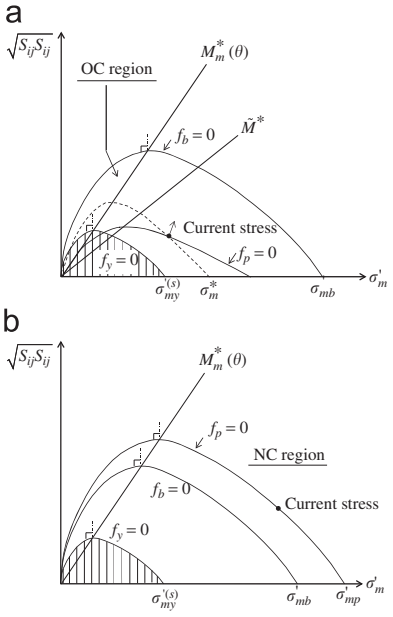

Fig. 2. Overconsolidation boundary surface, static yield function, and potential function. (a) OC region and (b) NC region.

both the overconsolidated region and the normally consolidated region.

Based on the overstress type of viscoplastic theory first adopted by Perzyna (1963), viscoplastic strain rate tensor $\dot{\varepsilon}_{ij}^{vp}$ is defined as

$$\dot{\varepsilon}_{ij}^{vp} = C_{ijkl}\langle \Phi(f_y)\rangle \frac{\partial f_p}{\partial \sigma'_{kl}} \tag{18}$$

$$\langle \boldsymbol{\Phi}(f_y)\rangle = \begin{cases} \boldsymbol{\Phi}(f_y): & f_y > 0 \\ 0: & f_y \le 0 \end{cases} \tag{19}$$

$$C_{ijkl} = a\delta_{ij}\delta_{kl} + b(\delta_{ik}\delta_{jl} + \delta_{il}\delta_{jk}) \tag{20}$$

where $\langle\ \rangle$ are Macaulay's brackets, $\Phi(f_y)$ is the rate-sensitive material function, and C_{ijkl} is a fourth order isotropic tensor. a and b in Eq. (20) are the viscoplastic parameters. $\Phi(f_y)$ is determined from the experimental correlation proposed by Adachi and Oka (1982) and Kimoto and Oka (2005) as

$$\boldsymbol{\Phi}(f_y) = \sigma'_m \exp\left\{ m'\left(\overline{\eta}^*_{(0)} + \tilde{M}^* \ln\frac{\sigma'_m}{\sigma'_{mb}}\right)\right\} \tag{21}$$

in which m' is the viscoplastic parameter.

Deviatoric viscoplastic strain rate $\dot{e}_{ij}^{vp}$ and volumetric viscoplastic strain rate $\dot{\varepsilon}_{kk}^{vp}$ can be expressed as

$$\dot{e}_{ij}^{vp} = C_1 \exp\left\{ m'\left(\overline{\eta}^*_{(0)} + \tilde{M}^* \ln\frac{\sigma'_m}{\sigma'_{mb}}\right)\right\} \frac{\eta^*_{ij} - \eta^*_{ij(0)}}{\overline{\eta}^*} \tag{22}$$

$$\dot{\varepsilon}_{kk}^{vp} = C_2 \exp\left\{ m'\left(\overline{\eta}^*_{(0)} + \tilde{M}^* \ln\frac{\sigma'_m}{\sigma'_{mb}}\right)\right\}\left\{ \tilde{M}^* - \frac{\eta^*_{mn}(\eta^*_{mn} - \eta^*_{mn(0)})}{\overline{\eta}^*}\right\} \tag{23}$$

where $C_1 = 2b$ and $C_2 = 3a + 2b$ are the viscoplastic parameters for the deviatoric and the volumetric strain components, respectively.

3.2. Strain-dependent elastic shear modulus

The non-linearity of soil stiffness has been studied extensively for materials such as sand, clay, and gravel, and has been summarized well by Ishihara (1996). Considering the effect of both the confining pressure and the strain dependency of the shear modulus, a normalized shear modulus reduction function based on the viscoplastic shear strain is given by

$$G = G_0 \frac{1}{(1 + \alpha(\gamma^{vp})^r)} \sqrt{\frac{\sigma'_m}{\sigma'_{m0}}} \tag{24}$$

where α is the strain-dependent parameter and r is the experimental constant, which is chosen as $r = 0.4$ based on the experimental results (Ogisako et al., 2007). γ^{vp} is the accumulated viscoplastic shear strain given by the viscoplastic deviatoric strain increment as $\gamma^{vp} = \int \sqrt{de_{ij}^{vp} de_{ij}^{vp}}$.

It is worth noting that G_0 also depends on the void ratio, as shown by Hardin and Black (1968).

3.3. Finite element method formulation

In the numerical simulation, the finite element method for two-phase mixtures, based on the finite deformation theory and updated Lagrangian method, is adopted with the objective Jaumann rate of Cauchy stress for the weak form of the equilibrium equation (Oka et al., 1992, 2002a; Kimoto et al., 2004). A Biot's type of two-phase mixture theory is used with a velocity–pore pressure formulation. The grain size particles and the fluid are assumed to be incompressible. An eight-node quadrilateral isoparametric element with reduced Gaussian four-point integration is employed for the displacement. The pore water pressure is defined by a four-node quadrilateral isoparametric element. The details of the adopted finite element formulations can be found in Higo et al. (2006).

3.4. Construction procedure and loading profile

The linearized construction sequence for the super levee is schematically shown in Fig. 3. The rate of loading is simulated by the successive addition of elements corresponding to each stage of the embankment construction. In this figure, the symbols show the assumed construction layer/stage of each embankment. For a particular construction stage, the elements to be constructed are added and given a constitutive model appropriate to the material behavior during placing. The nodal force due to the self-weight body forces of the constructed material are calculated and applied to the corresponding nodes. The global stiffness matrix and all the other boundary conditions are assembled for the stage, and the finite element analysis is implemented. Before applying the next stage, the displacements of any nodes, which are only connected to the constructed elements, are zeroed. The procedure for the construction of the other stages follows similar steps. The final results are obtained by the accumulated results of each stage of the analysis (Potts and Zdravkovic, 1999).

The construction of the super levee was begun by placing the main levee fill material in eight layers consecutively within 5 months. The construction was carried out by extending the back slope immediately after the completion of the main levee in six layers up to a maximum height of 6.3 m during a period of 4 months. After construction was suspended for 13 months, and time was allowed for a short-time consolidation, the procedure was then followed through to the final level by the placing of two layers in 5 months. Hence, the super levee was completed in a total of 27 months. As shown in Fig. 3, consolidation analyses are continued for 10 years after the completion of the super levee in order to consider the long-term behavior of such embankments on soft clay deposits.

3.5. Problem geometry and boundary conditions

The geometry and the boundary conditions of the finite element analyses are presented in Fig. 4. The size of the model domain is determined so that the boundary effect

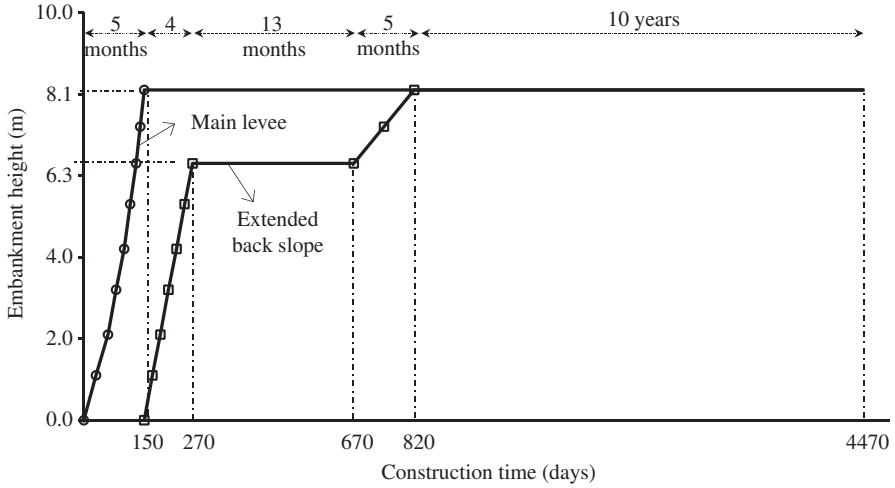

Fig. 3. Construction sequence for the super levee and consolidation time after its completion.

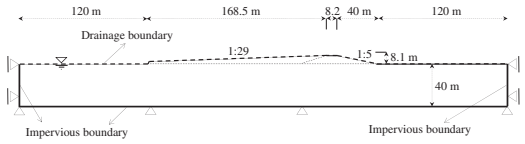

Fig. 4. Geometry and boundary conditions for the finite element model (final shape after completing the construction).

can be minimized. Fully saturated conditions are assumed with a drainage boundary only at the top. The displacement boundary at the bottom of the domain is fixed in both horizontal and vertical directions, while the two side boundaries are fixed only in the horizontal direction. The initial effective stress conditions of the ground layers are assigned at the outset of the analysis based on the unit weight of the subsurface layers. The embankment layers are directly simulated in the finite element analyses following the construction sequence presented in Fig. 3.

4. Modeling of the natural (unimproved) ground case

The consolidation analysis of the super levee construction on a natural ground has been performed to study the effect of destructuration, demonstrated as structural degradation and the strain-dependent elastic shear modulus, on the long-term consolidation behavior. The destructuration is delineated by structural degradation in the elasto-viscoplastic constitutive model. The structural degradation has been expressed as strain softening with respect to the accumulation of viscoplastic strain, so that the model can describe the instability not only around the failure stress, but also during the compressive deformation. On the other hand, the non-linearity of the elastic shear modulus is taken into consideration as another aspect of destructuration, as explained in Section 3.2.

Laboratory tests have been performed on specimens obtained from the in situ sampling procedure, including undrained triaxial compression tests and consolidation tests. The consolidated undrained triaxial tests have been performed with two different strain rates, namely, 0.05%/min and 0.005%/min, and at three levels of consolidation pressure equal to 100, 200, and 400 kPa for different samples.

For all layers, the soil parameters are determined in a reasonably simple and robust manner from laboratory tests on the obtained samples, except for some layers for which there was a lack of adequate experimental data, and thus, a set of available data from similar sites were properly chosen. The material parameters for the elasto-viscoplastic model are determined from the laboratory test results using the proposed method by Kimoto and Oka (2005). As shown by Kimoto and Oka (2005), the visco-plastic parameters can be determined by undrained triaxial tests with different strain rates. Based on the soil properties, soft clay layer Ac2 is divided into three individual sub-layers, namely, upper sub-layer Ac2-U, middle sub-layer Ac2-M, and lower sub-layer Ac2-L. The representative material parameters for the embankments and the subsurface layers are listed in Table 1. Taking into account the fact that the strain dependency of the shear modulus alters the values of the structural parameters, the modified values for β are presented in Table 1 as well.

In order to determine the effect of each aspect of destructuration on the behavior of the soft clay specimens obtained from layer Ac2, the modeling under undrained triaxial conditions is performed by the integration of the elasto-viscoplastic constitutive equations. Fig. 5 presents the stress–strain relations and the stress paths of the soft clay specimens from layer Ac2-M, with structural degradation, before and after consideration of the strain dependency of the shear modulus. The laboratory test results are depicted by the symbols in Fig. 5 for different levels of confining pressure, while the corresponding predicted results are shown by the solid lines. The graphs located on the left side represent the case before the strain dependency is considered ($\alpha=0$), while the graphs located on the right side show the simulated results after the strain dependency is considered. The effect of structural

Table 1
Material parameters for the embankments and the ground layers for the natural ground case.

Layers	Parameters													
	k (m/s)	γ_t (kN/m^3)	e_0	υ	σ'^{a}_{m0} (kPa)	G_0^b (kPa)	λ	κ	M^*_{mc}	m'	C_1,C_2 (1/s)	n	β	α
Em2	1.00×10^{-5}	18.0	0.8	0.3	10.0	5385								
Em1	1.00×10^{-5}	17.5	0.8	0.3	10.0	4310								
B1	1.00×10^{-5}	17.5	0.93	0.28	10.0	3300								
As2	7.37×10^{-6}	18.0	0.84	0.285	31.3	5375								
Ac2-U	5.75×10^{-10}	17.0	1.25		63.8	3760	0.341	0.019	1.24	24.68	3.83×10^{-11}	0.83	5,10[c]	20
Ac2-M	3.85×10^{-10}	16.0	1.65		80.4	3930	0.593	0.027	1.18	28.2	1.85×10^{-11}	0.67	10,15[c]	10
Ac2-L	2.69×10^{-10}	16.6	1.42		108.0	5995	0.652	0.014	1.12	21.25	8.99×10^{-11}	0.60	15,20[c]	10
As1	5.55×10^{-6}	18.0	0.9	0.3	119.0	6465								
Ac1	1.60×10^{-9}	16.0	1.30		153.0	3540	0.326	0.0326	1.12	20.0	3.00×10^{-12}	0.70	10,10[c]	10
Dg	1.00×10^{-5}	19.0	0.9	0.3	161.0	40920								
Dc	5.30×10^{-10}	18.0	1.20		183.0	7695	0.217	0.0217	1.30	20.0	1.16×10^{-13}	0.70	10,10[c]	10

[a]The approximate value at the center of each layer. The value of 10 kPa is assigned as the minimum for the surface layers.
[b]Based on the mean effective stress at depth of each layer.
[c]Modified values after strain-dependent shear modulus consideration.

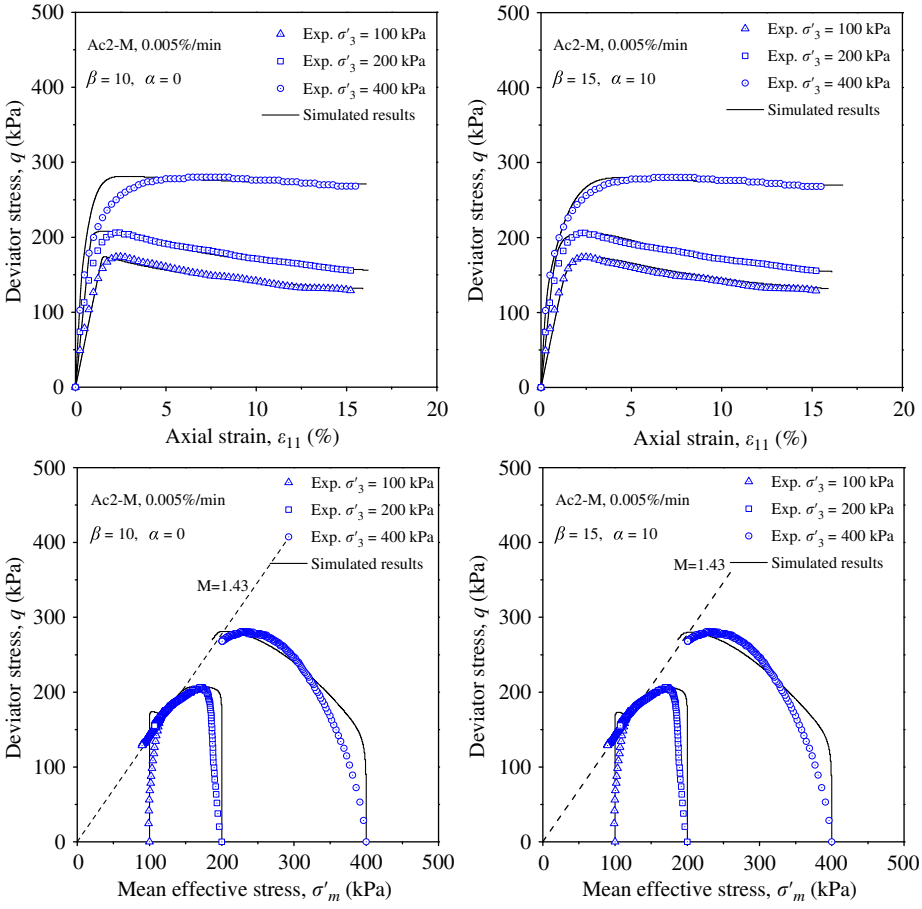

Fig. 5. Stress–strain relations (above) and stress paths (below) of Ac2-M soft clay specimens during triaxial tests and the simulated results. In the stress paths, the stress ratio is obtained as $M=(q/\sigma'_m)_{failure}$.

degradation on the stress–strain relations has been demonstrated by Kimoto and Oka (2005) as the strain softening behavior just after the peak stress point, in which the larger structural parameter β promotes the rapid degradation of the shear strength. The inclusion of the strain dependency of the shear modulus in the modeling significantly improves the behavior before the peak stress point at the early stages of loading, by which the predicted results are

found to be in notable agreement with the experimental ones. In contrast to the stress–strain relations, the effect of the strain-dependent shear modulus on the stress paths under triaxial conditions is not significant.

Evaluating the effects of soft clay destructuration on the super levee consolidation analysis, three cases are simulated on the natural ground, namely, Case N1 without any consideration given to either the structural degradation or the strain dependency of the shear modulus, Case N2 with consideration given only to the structural degradation, and Case N3 with consideration given to both the structural degradation and the strain dependency of the shear modulus. All the cases assume the same initial conditions, in which only structural parameter β and strain-dependent parameter α are subject to change. The material parameters summarized in Table 1 are used in the simulations in which the elastic behavior is assumed for the sand and the gravel layers and the elasto-viscoplastic constitutive model is applied for the clay layers.

5. Modeling of the improved ground case

The consolidation analysis of the super levee on the improved foundation is conducted based on the improvement techniques performed at the Torishima site, namely, deep mixing walls, sand drains, and sand compaction piles. The temporary effects of each improvement technique during the installation procedure, such as changes in stress in the surrounding soil and the development of excess pore water pressure, are disregarded in this study. Efforts are made to simulate each improvement technique inasmuch as its substantial function can be effectively represented in the two-dimensional analysis. The simulation for this case is conducted by considering the effect of both the structural degradation and the strain dependency of the shear modulus on the clayey layers, so the results can be compared to those in Case N3 for the natural (unimproved) ground.

The initial stress conditions are determined in a similar manner as for the unimproved ground case. The initial stress state is considered regardless of temporary changes in stress during and a while after the installation of the DM, SD, and SCP, since the exact effect of each technique on the variation in stress during installation is not clarified. It means that the steady state after the execution of ground improvement techniques is taken as the initial stress state of the ground layers, and the changes in stress due to temporary variations in the pore water pressure, the densification, the disturbance of the surrounding soils and so on are ignored.

The effective stress conditions after the ground improvement are considered as the initial configuration. For that purpose, the finite element mesh of the ground layers, including the corresponding elements of DM, SD, and SCP, is developed and the initial stress state is computed by the static elasto-perfectly plastic analysis using the Drucker–Prager type material model.

5.1. Simulation of deep mixing walls under plane-strain conditions

Deep mixing is an in situ ground-improvement technique which mixes in situ soil with a cementitious agent (mainly cement slurry or powder) by augers to improve the engineering characteristics of the soil. This technique has been used to mitigate potential damage to levees by enhancing the overall stiffness and reducing the permeability of the soil. In the two-dimensional plane-strain model, deep mixing walls are directly modeled in the finite element mesh based on the actual size and spacing, whilst for the surrounding parts in between the DM walls, the equivalent material parameters are estimated and assigned. The characteristics of the composite ground treated with deep mixing walls can be well represented by the estimated equivalent parameters. Fig. 6 shows the conversion of the 3D deep mixing wall pattern into the equivalent plane-strain model. The equivalent stiffness of the soil–DM composite is calculated using the stiffness of the deep mixing walls and the stiffness of the natural soil with the respective area improvement ratio as

$$E_{composite,DM} = E_{DM} \times a_{s,DM} + E_{soil} \times (1 - a_{s,DM}) \tag{25}$$

where $E_{composite,DM}$ is the equivalent stiffness of the soil–DM composite, E_{DM} is the DM wall stiffness, E_{soil} is the natural soil stiffness, and $a_{s,DM}$ is the area improvement ratio for the surrounding parts amid the DM walls. The deep mixing walls have been installed mainly in the sandy layers, as shown in Fig. 1. Therefore, the equivalent vertical permeability is estimated based on Darcy's law as

$$k_{v,composite} = k_{DM} \times a_{s,DM} + k_{soil} \times (1 - a_{s,DM}) \tag{26}$$

in which $k_{v,composite}$ is the equivalent vertical permeability of the soil–DM composite, k_{DM} is the permeability of the deep mixing walls, and k_{soil} is the permeability of the natural soil. In the same manner, the equivalent horizontal permeability of the soil–DM composite is assumed to be equal to the permeability of the DM walls as the part with lower permeability ($k_{h,composite} = k_{DM}$).

According to the DM wall pattern in the Torishima super levee project (Kinki Regional Development Bureau, 2009), a respective area improvement ratio $a_{s,DM}$ of 30% for the composite parts amid the DM walls is obtained. Following Eqs. (25) and (26), the characteristic parameters of the soil–DM composite zone can be determined. The properties of the DM walls are subsequently obtained from

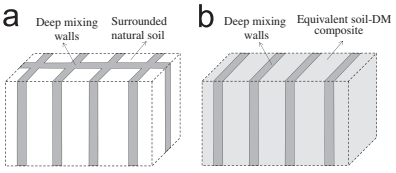

Fig. 6. Conversion of the deep mixing walls in a 3D pattern into the plane-strain model. (a) Deepmixing walls in 3D pattern, and (b) plane-strain model of deep mixing walls and composite parts.

the existing data in a similar case study conducted by Oka et al. (2002b).

During the large deformation of the ground, a large rotation may occur. Since Darcy's law is not objective, but merely an approximation (Eringen, 2003), and since the kind of effect the rotation has during the deformation has not been clarified, the effect has not been considered.

5.2. Simulation of sand drains under plane-strain conditions

Vertical drains accelerate the rate of settlement and reduce the excess pore water pressure which may cause a risk to the stability of the embankment slopes. Several methods have been proposed for the simulation of sand drains in plane-strain models (e.g., Cheung et al., 1991; Hird et al., 1992; Indraratna and Redana, 1997; Chai et al., 2001). Hird et al. (1992) developed a matching procedure which can be achieved by adjusting the drain spacing (geometry) and/or the permeability of the soil. The proposed method includes the effects of smear zones around the drains without any requirement for separate discretization.

In order to employ a realistic 2D finite element analysis for vertical drains, an equivalence between the plane-strain analysis and the 3D axisymmetric analysis needs to be established. The spatial vertical drain system, with effective drainage radius R, should be converted into the equivalent infinitely parallel drain wells located at a spacing of $2B$, for which B is the half-width of a plane-strain unit cell. The conversion of an axisymmetric sand drain unit into the plane-strain approximation is schematically shown in Fig. 7, where l is the length of a drain unit cell, and r_w and r_s are the radius of the drain and the radius of the smear zone in an axisymmetric unit, respectively. b_w is the half-width of the sand drain under plane-strain conditions. Following the Hird et al. (1992) method, the relationship between the horizontal permeability of plane-strain condition k_{hpl} and the horizontal permeability of axisymmetric unit cell k_{hax} is given by

$$\frac{k_{hpl}}{k_{hax}} = (B^2/R^2) \times \left(\frac{2}{3[\ln(n/s) + (k_{hax}/k_s)\ln(s) - 0.75]} \right) \quad (27)$$

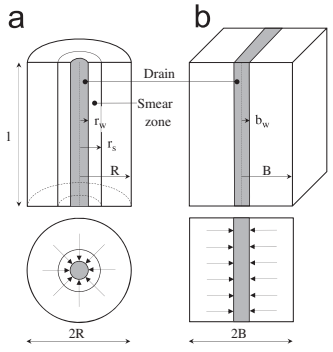

Fig. 7. Conversion of the axisymmetric sand drain unit into the plane-strain model. (a) Axisymmetric radial flow, and (b) plane-strain.

where $n=(R/r_w)$ and $s=(r_s/r_w)$. k_{hax} and k_s are the horizontal permeability outside and inside the smear zone, respectively. The modified horizontal permeability of the soil within the sand drains in the plane-strain model is obtained based on the in situ horizontal permeability of the soil and considers the size and the permeability of the smear zone. By setting B to a desired value in Eq. (27), a different geometry for the sand drain can be assigned under the plane-strain conditions. This becomes useful when keeping similar drain spacing between the two systems and leads to an excessively large number of elements in the finite element analysis.

In the present study, the sand drains are represented in the plane-strain model by applying additional drainage boundary conditions to the nodes of the mesh at the locations of the sand drains instead of including separate elements to represent the sand material ($b_w=0$). This method is adopted to prevent any computational instability which may easily occur by putting the narrow elements as sand drain material in the finite element mesh. Representing the sand drains as boundary conditions implies that the sand drains provide ideal drains with no additional resistance to embankment loading. Concerning the permeability-matching procedure, described in Eq. (27), the plane-strain drain spacing is assumed as $B=2R$ and the size of the smear zone is assumed as $s=(r_s/r_w)=2$. The permeability of the smear zone, term k_{hax}/k_s, is considered to be determined from the preloading process results.

5.3. Simulation of sand compaction piles under plane-strain conditions

The sand compaction pile (SCP) method has been widely used in construction to form compacted sand piles in a soft ground by vibration, dynamic impact, or static excitation. The principle of this ground improvement technique is the densification of the ground, which leads to an increase in soil density as well as an increase in lateral effective stress. Besides the strengthening effect of the SCP method, the drainage function of sand compaction piles is considered to enhance the resistibility of soft clay deposits by accelerating the rate of consolidation.

In the current study, as sand compaction piles have been installed only in the sandy layers, the drainage effect of the piles themselves is disregarded. For the locations at which the sand compaction piles are installed on top of the sand drains, the drainage effect is preserved by substituting the sand compaction piles with sand drains that are connected underneath. In order to include the strengthening effect of SCPs in the finite element simulation, the simplified homogenization method is adopted to avoid a large number of elements which may be produced by directly modeling the piles as discrete elements.

For the SCP installation zone, if we follow the same procedure as for the DM, we have the equivalent stiffness

of the improved zone as

$$E_{composite,SCP} = E_{SCP} \times a_{s,SCP} + E_{soil} \times (1 - a_{s,SCP}) \quad (28)$$

The area improvement ratio of SCP-improved zone $a_{s,SCP}$ is about 10%. In addition, the stiffness of the SCPs is not remarkably larger than the stiffness of the surrounding soil. Therefore, the equivalent stiffness by this method would not be very different from the original soil stiffness. On the other hand, the main function of sand compaction piles in loose sandy layers is the densification of the surrounding soil. The densification has a significant effect on the stiffness of the surrounding soil. Accordingly, due to the lack of adequate field data, a simplified homogenization method is considered in which the stiffness of the SC piles themselves is disregarded and the densification effect of the SCPs on the surrounding soil is considered as the main function. To evaluate the effect of ground densification by SCPs, the SPT blow count before and after improvement was employed. Therefore, the stiffness of the ground layers is approximated linearly according to the changes in N_{SPT}. Following Uto (1967), Young's modulus of the sand materials is estimated by N_{SPT} as

$$E\ (\text{kPa}) = 2800 N_{SPT} \quad (29)$$

According to the standard penetration test (SPT) results from the geotechnical site investigation, before and after the SCP installation, the stiffness of the SCP-improved zones is approximately 2.5 times the stiffness of the unimproved soil in the As2 layer. The equivalent permeability-matching procedure is applied in the SCP-improved zones based on the corresponding sand drain size and pattern. The other characteristic parameters are kept the same as those for the unimproved soil.

5.4. Parameter calibration based on the preloading monitored data

The excess preloading procedure was carried out by temporarily placing the fill material over the zones of the installed sand drains to improve the properties of the subsurface layers, particularly thick soft clay layer Ac2. The preloading procedure was initiated prior to the construction of the super levee, in two stages. At first, the fill material was placed in the whole area of preloading up to a height of 1.0 m within 10 days. After a suspension of 100 days, the fill height had risen to 3.0 and 7.0 m. The preloading scheme and the profiles are plotted schematically in Fig. 8 within the sketch of the super levee cross section. During the preloading procedure, the settlements at the ground level were observed at several points simultaneously. The locations of the recorded points for the current cross section are also depicted in Fig. 8 with the distances from the left toe of the main levee.

Based on the preloading profiles, finite element simulations are conducted for the consolidation analyses during the preloading process. The equivalent material parameters

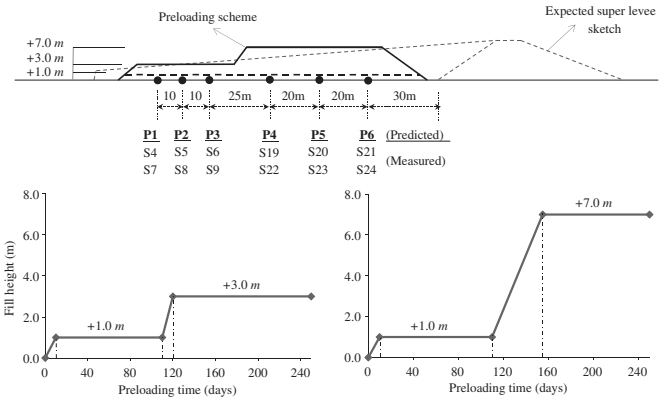

Fig. 8. Preloading scheme and profiles with the location of the settlement observing points during the preloading procedure.

for the improved zones are calculated using the proposed methods for each ground-improvement technique. For the clay materials, the parameters are allocated after considering the strain-dependent shear modulus. Since the preloading procedure is performed mainly to improve the characteristics of the clay layers within the sand drains by pre-consolidation, efforts are made to approximate the appropriate properties of the Ac2 layers after the sand drain installation and the preloading procedure. Two main factors are determined herein, namely, the permeability of the smear zone as k_{hax}/k_s and viscoplastic parameters C_1 and C_2 in the Ac2 sub-layers within the sand drains. Through the progression of the consolidation and the discharge of excess pore water pressure through the sand drains, the performance of the sand drains may be reduced in time due to the fine particles entering the drainage channel known as the clogging. This effect is speculated here by changing the permeability of the smear zone. On the other hand, the viscoplastic parameters obtained from the laboratory test data may be different from the actual field values. Several reasons can be given for this, such as the disturbance and the stress release of the soil specimens during the sampling procedure, the higher applied stress rate in the laboratory tests, and the different stress histories which the soil has experienced in the field. In addition, the installation of the sand drains and the consequent fabric changes in the clay layer can particularly affect the viscoplastic parameters. Considering the uncertainty of the viscoplastic parameter values obtained from the experimental results and the effect of the sand drain installation, changes in the viscoplastic parameters are expressed by the CI index. Viscoplastic parameters C_1 and C_2 are obtained to be identical in this study; therefore, the CI index is defined as $CI = (C_1^{Improved}/C_1^{Natural})$.

Comparisons are made through the settlement profiles at the ground level with the field observed data. Fig. 9 shows the settlement-time profiles under a preloading of +3.0 m, at the field monitored points and the corresponding points in the simulations. The field observed data are displayed by symbols and the predicted ones are shown by lines. As

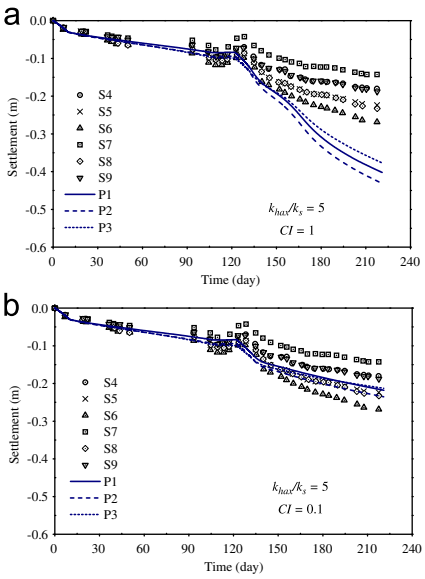

Fig. 9. Settlement-time profiles at the ground level for the points under +3.0 m preloading: (a) $CI=1$, and (b) $CI=0.1$ (S4–S9 the field data points, P1–P3 the predicted data points).

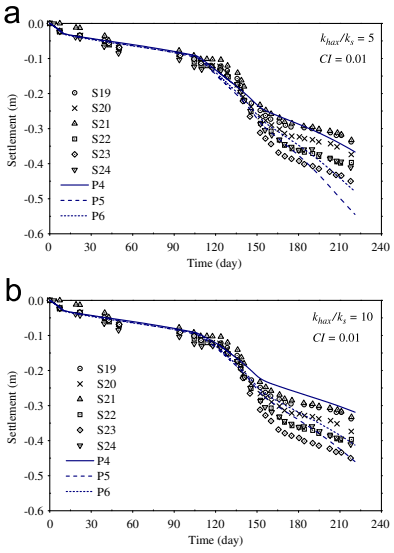

Fig. 10. Settlement-time profiles at the ground level for the points under +7.0 m preloading: (a) $(k_{hax}/k_s)=5$, and (b) $(k_{hax}/k_s)=10$ (S19–S24 the field data points, P4–P6 the predicted data points).

illustrated in Fig. 9(a), the analysis is initiated with $CI=1$ and $(k_{hax}/k_s)=5$, wherein the predicted results are larger than the field observed data. Therefore, the analysis is carried out by reducing the viscoplastic parameter index as $CI=0.1$, shown in Fig. 9(b). Taking a smaller viscoplastic parameter for the soft clay layers, Ac2, results in a better agreement with the field observed data, since the pre-consolidation of the clay layers subjected to preloading is in progress. In the analyses under a preloading of +7.0 m, and following the same +3.0 m preloading analyses, at first the reduced viscoplastic parameter of $CI=0.01$ is adopted with $(k_{hax}/k_s)=5$. However, as shown in Fig. 10(a), the predicted results exhibit rather larger values than the field data. Therefore, the permeability of the smear zone is adjusted to $(k_{hax}/k_s)=10$ in order to achieve more precise values in the prediction results by slightly reducing the rate of the consolidation-induced settlement, as shown in Fig. 10(b).

As the main deformations are expected to develop under the higher embankment level, and also considering the long-term behavior of the super levee, the results of the +7.0 m preloading analysis are assigned for further analyses of the improved ground case. Accordingly, the final material parameters for the subsurface layers are obtained by assuming $(k_{hax}/k_s)=10$ and $CI=0.01$. Table 2 presents the additional material parameters which are used for the improved case analysis. *CI* is affected by deformation history before loading. The permeability coefficient also depends on the deformation history. Since a detailed construction procedure is not known, this parameter has been determined using the preloading results. It is preferable to determine CI using the tests on samples of natural and improved soil.

During the sand drain installation, the surrounding soil just near the SD is partially compacted. This zone is called a smear zone. A smear zone is created in a sand drain by the remolding of clay during the drilling operation for building it. Smear zones have lower permeability than the original clay. Based on the SD spacing in the FE mesh, this lower permeability of the smear zones can result in smaller equivalent permeability for the whole SD/soil composite. As shown in Eq. (27), the permeability under plane-strain conditions k_{hpl} varies with SD spacing B in the FE mesh. For the values of B smaller than about $3R$, the equivalent permeability is smaller than the permeability of the original clay. In the current analysis, $B=2R$ is taken, which results in $k_{hpl}/k_{hax}=0.35$. For the determination of permeability, it is preferable to conduct permeability tests on both natural and improved grounds.

6. Simulation results and discussion

6.1. Vertical displacements

In Fig. 11, the overall vertical displacements at the ground level are presented in various stages, during and after construction, for both natural ground and improved ground cases. The vertical displacements are plotted as settlements versus X coordinate from the left-side boundary. In general, all the cases present quite similar features. The trough-shaped settlements beneath the main levee with upward heaves adjacent to the main levee are observed at an earlier stage of construction. Continuing the construction in the back slope, the settlements develop beneath that part and increase during consolidation. The surface heaves around the toe of the embankments and shows an upward movement during construction, which turns downward after the completion of the construction.

Comparing the vertical displacements for the natural ground cases at the end of the construction (EOC) in 27

Table 2
Additional material parameters for the ground layers for the improved ground case after the preloading process calibration.

Layers	Parameters											
	k (m/s)	γ_t (kN/m^3)	e_0	G_0 (kPa)	λ	κ	M^*_{mc}	m'	C_1,C_2 (1/s)	n	β	α
DMW /sand	9.80×10^{-9}	20.0	0.72	81155								
DMW/Clay	5.75×10^{-11}	20.0	0.72	81155								
B1-DM	7.00×10^{-6}	18.75	0.8	27040								
B1-SCP	k_x: 3.55×10^{-6}	17.5	0.93	13480								
As2-DM	5.16×10^{-6}	19.0	0.72	28065								
As2-SCP	k_x: 2.62×10^{-6}	18.0	0.84	13430								
As2-SD	k_x: 2.62×10^{-6}	18.0	0.84	5375								
Ac2-U-DM	4.20×10^{-10}	18.5	1.25	26980								
Ac2-U-SD	k_x:2.04×10^{-10}	17.0	1.25	3760	0.341	0.019	1.24	24.68	3.83×10^{-13}	0.83	10	20
Ac2-M-SD	k_x:1.37×10^{-10}	16.0	1.65	3930	0.593	0.027	1.18	28.2	1.85×10^{-13}	0.67	15	10
Ac2-L-SD	k_x:9.55×10^{-11}	16.6	1.42	5995	0.652	0.014	1.12	21.25	8.99×10^{-13}	0.60	20	10
As1-SD	k_x: 1.97×10^{-6}	18.0	0.9	6465								

k_x: Equivalent horizontal permeability.

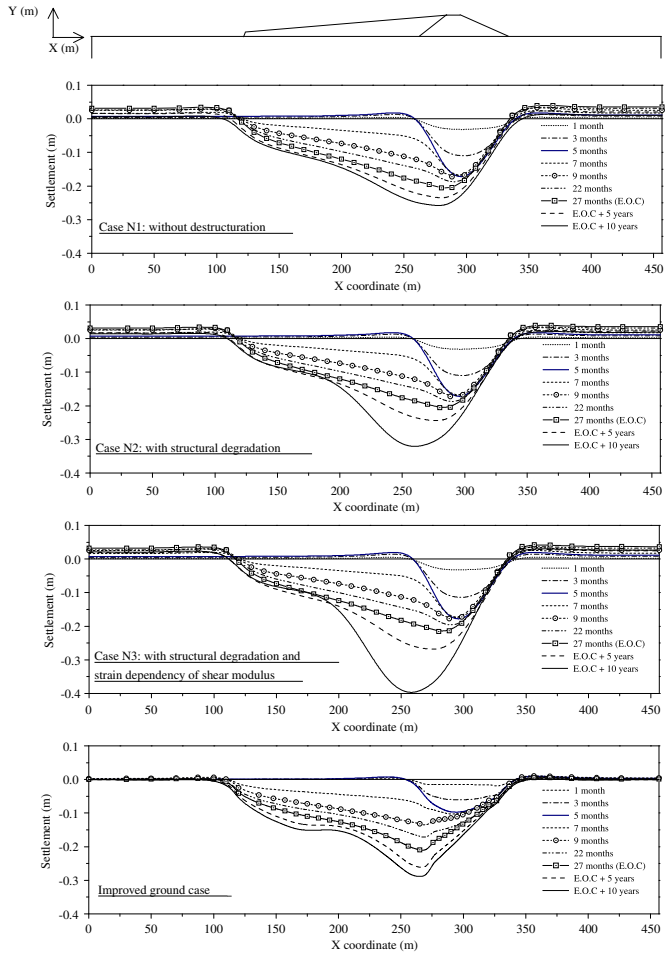

Fig. 11. Ground level settlement profiles during loading and consolidation for the natural ground cases (Cases N1, N2, and N3) and the improved ground case.

months, Cases N1 (without destructuration) and N2 (with structural degradation) demonstrate almost similar settlements, while Case N3 (with structural degradation and strain dependency of the shear modulus) exhibits relatively larger settlements. This fact indicates the effect of the strain dependency of the shear modulus on the deformations during the loading process. During consolidation, however, as the structural degradation is taken into account for Cases N2 and N3, larger settlements develop because of strain softening in the soft clay layers. It is interesting to note that in the natural ground cases, N1, N2, and N3, the ground heaves more for EOC+10 years than EOC+5 years around $X=125$–200 m. This might be due to a deformation mode, such as volumetric strain localization. Comparing the vertical displacements for the improved ground case and Case N3, the improved ground case exhibits the same features in terms of the ground level settlement, although the predicted surface heaves around the embankment toes are quite small. The settlements beneath the main levee become smaller than those in Case N3, as DM walls have been installed underneath. The effect of SCP/SD is observed as accelerating the rate of consolidation by shortening the drainage paths, in which the generated excess pore water pressure and subsequent deformations are reduced.

The settlement versus time at $X=260$ m, which represents the location of the maximum overall settlement in most of the cases, is plotted in Fig. 12 in a logarithmic scale. The effect of the structural degradation and the strain dependency of the shear modulus can be clearly observed among the natural ground case results. The displacement rate in Case N3 starts with larger values in the surface heave and the settlement compared to those in Cases N1 and N2, which have similar displacement rates during the construction process. After that, the rates of displacement in Cases N2 and N3 increase due to structural degradation during consolidation and result in larger settlements. In the improved ground case, the vertical displacement appears as settlement in an earlier stage of construction, despite the surface heave in the natural ground cases. Furthermore, the effect of the installation of sand drains at this location is observed as a higher rate of displacement during construction, which is reduced during the long-term consolidation and results in smaller settlements compared to Case N3.

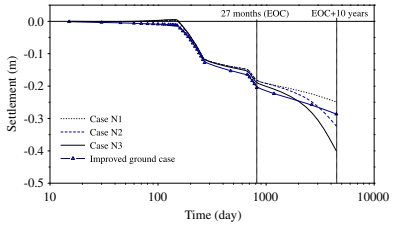

Fig. 12. Ground level settlement versus time at $X=260$ m for the natural ground cases (Cases N1, N2, and N3) and the improved ground case.

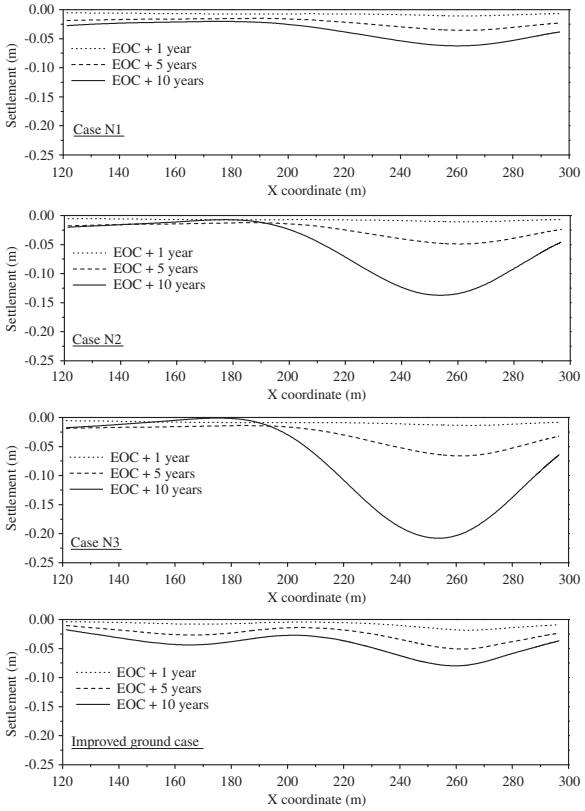

Fig. 13. Settlement profiles atop the super levee after the end of the construction (EOC), for the natural ground cases (Cases N1, N2, and N3) and the improved ground case.

The predicted vertical displacements atop the super levee after the end of the construction are presented in Fig. 13 for different cases. The vertical displacement on top of the super levee shows a similar trend to that for the ground level settlements, but with smaller values in general. The locations of the maximum settlement atop the super levee in different cases nearly corresponded with the locations of the settlements in the ground level. For the natural ground cases, the settlements 1 year after EOC are almost similar for Cases N1, N2, and N3. Afterwards, however, the effect of structural degradation within the consolidation process becomes more evident and leads to relatively larger settlements in Cases N2 and N3. In the improved ground case, as pre-consolidation with sand drain installation has been carried out, a smaller settlement develops compared

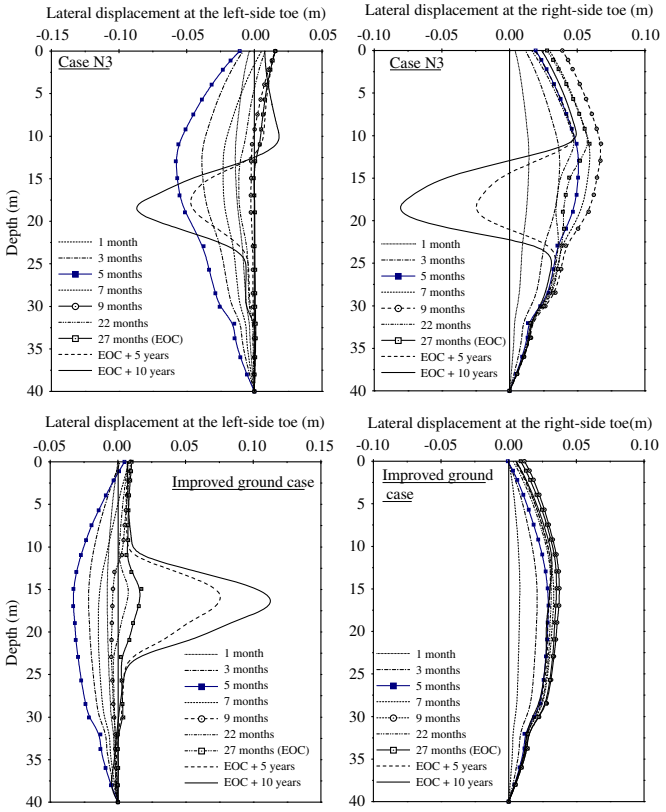

Fig. 14. Lateral displacement profiles at the main levee toes along the ground depth for natural ground Case N3 and the improved ground case.

to Case N3. Nonetheless, the notable relative settlement is still observed throughout the surface of the super levee.

6.2. Lateral displacements

The lateral displacements at the left- and the right-side toes of the main levee along the ground layers are illustrated in Fig. 14 for Case N3 and the improved ground case. The other natural ground cases demonstrate variations nearly similar to those of Case N3; therefore, the results for Case N3 are only presented here to evaluate the effect of the ground-improvement techniques on the lateral displacements. In the consolidation of the embankment construction, the lateral displacement along the toe follows the process of excess pore pressure generation and dissipation under the embankment by forward and backward movements.

For Case N3, the lateral displacement at the right-side toe of the main levee is increased toward the right for 9 months with its maximum value at a depth of 11 m. Then it moves toward the left during the suspension of construction and consequent short-time consolidation. This sequence is continued by starting the next phase of construction and the following consolidation period. The maximum lateral displacement along the depth during the consolidation is observed at a depth of about 18 m, which is located in the Ac2 clay layer. At the left-side toe section, however, the lateral displacement presents rather different behavior, since the construction is carried out on both

sides of this section. At first, by constructing the main levee, it shows the lateral movement toward the left. However, by continuing the construction to the back slope, which is located on the left side of this section, slight rightward movements appear. During the long-term consolidation, the lateral displacement in this section follows the dissipation process of the generated excess pore pressure beneath the back slope, by showing leftward movements with a maximum value at a depth of about 18 m. This generation of the pore water pressure is associated with the development of viscoplastic volumetric strain in Ac2 layer shown in Fig. 17. This indicates that the lateral movements at the toes to the left are due to the large volumetric strain beneath the main levee.

For the improved ground case, at the right-side toe, the lateral displacement follows the same tendency as that for Case N3, but with smaller displacements due to the installation of the DM walls. At the left-side toe, similar movements occurred with smaller values while the surrounding soil is treated by the improvement techniques. During the long-term consolidation, the lateral displacement profile along the depth moves toward the right, following the dissipation of the generated excess pore pressure beneath the main levee.

6.3. Volumetric strain

The volumetric strain, which is calculated by the summation of the vertical and the horizontal strain, is

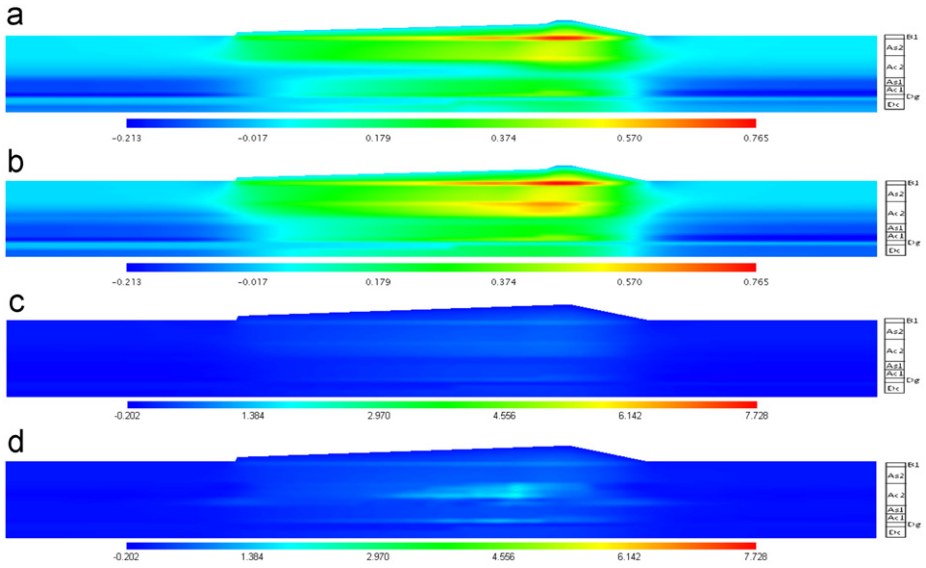

Fig. 15. Volumetric strain contours for Case N1 at various steps: (a) 9 months, (b) 22 months, (c) 27 months (EOC), and (d) 10 years after EOC (legend unit: %).

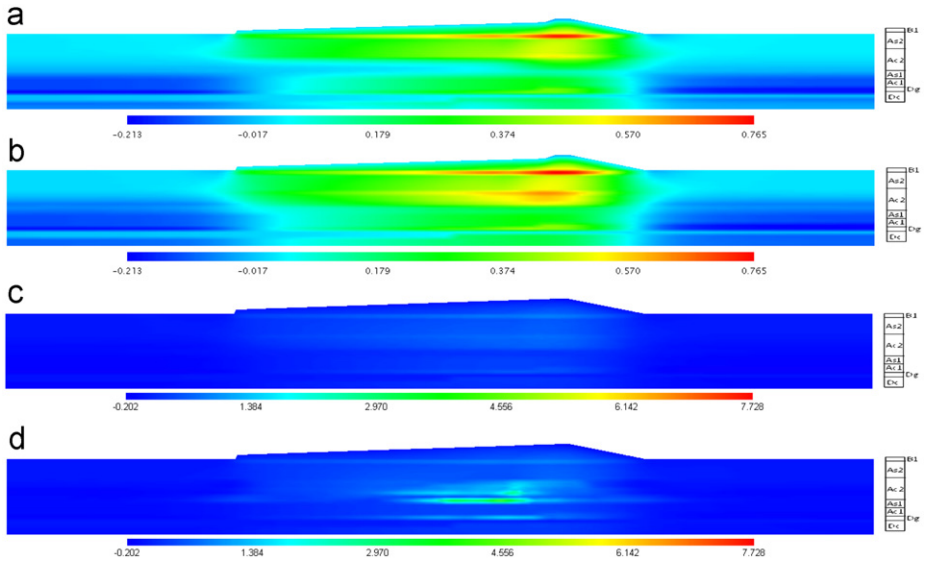

Fig. 16. Volumetric strain contours for Case N2 at various steps: (a) 9 months, (b) 22 months, (c) 27 months (EOC), and (d) 10 years after EOC (legend unit: %).

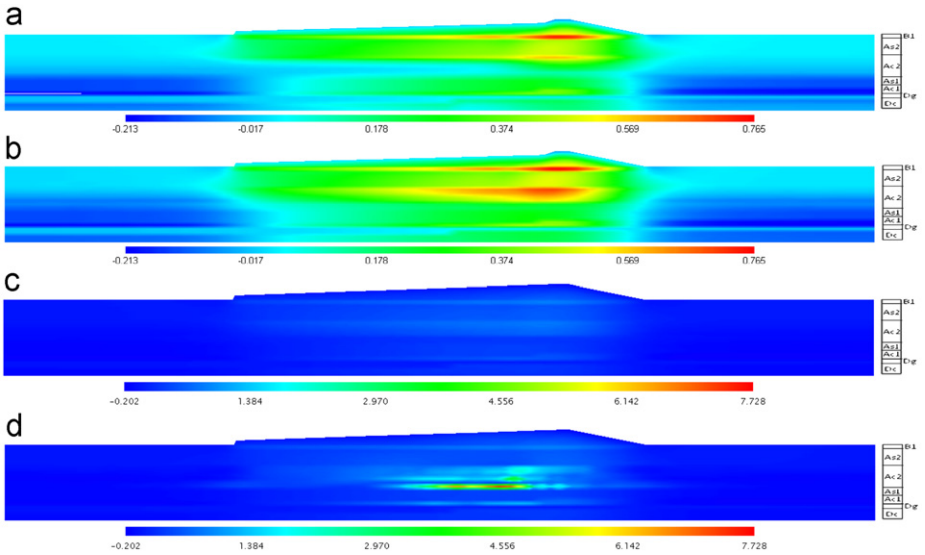

Fig. 17. Volumetric strain contours for Case N3 at various steps: (a) 9 months, (b) 22 months, (c) 27 months (EOC), and (d) 10 years after EOC (legend unit: %).

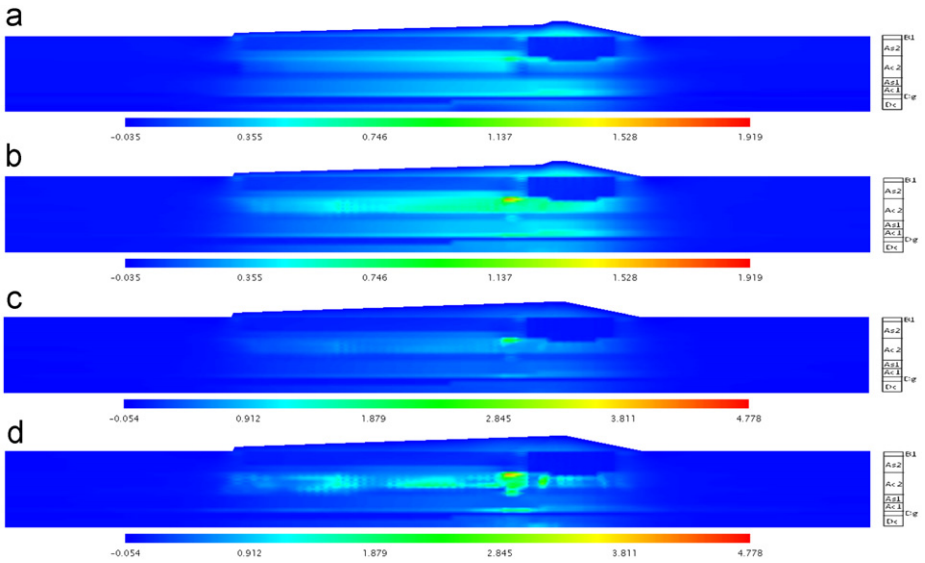

Fig. 18. Volumetric strain contours for the improved ground case at various steps: (a) 9 months, (b) 22 months, (c) 27 months (EOC), and (d) 10 years after EOC (legend unit: %).

shown in Figs. 15–18 for the three natural ground cases and the improved ground case, respectively. The volumetric strain contours at different stages of construction, namely, 9, 22, and 27 months, and 10 years after EOC are presented. As the volumetric strain changes over a wide range during the analysis, different legend scales are adopted in each case, accordingly.

After 9 months, Cases N1, N2, and N3 demonstrate nearly similar distributions of volumetric strain, with the strain localization mainly in the area just beneath the embankments and slightly at the upper part of the Ac2 clay layer. After 22 months, despite the similarity in the results for Cases N1 and N2, Case N3 shows a larger zone of strain localization in the Ac2 layer. Ten years after EOC, the volumetric strain localization is clearly observed in the Ac2 clay layers beneath the back slope for the three cases. A larger volumetric strain develops in Case N2 in comparison to that for Case N1, and the values of localized volumetric strain in Case N3 become even larger, because the strain dependency of the shear modulus is considered. The volumetric strains in the improved ground case, shown in Fig. 18, develop beneath the filling zones with smaller overall values compared to Case N3. However, significant strain localization is observed in the upper part of layer Ac2 in between the DM walls and the SCP/SD installation zones, in which about 5% of the volumetric strain is localized after 10 years of consolidation.

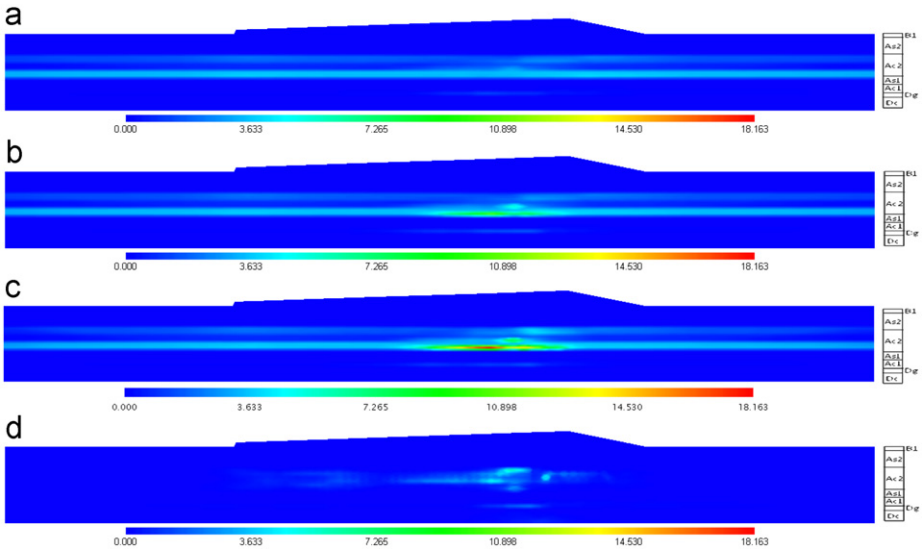

Fig. 19. Viscoplastic shear strain contours 10 years after EOC for different cases: (a) Case N1, (b) Case N2, (c) Case N3, and (d) the improved ground case (legend unit: %).

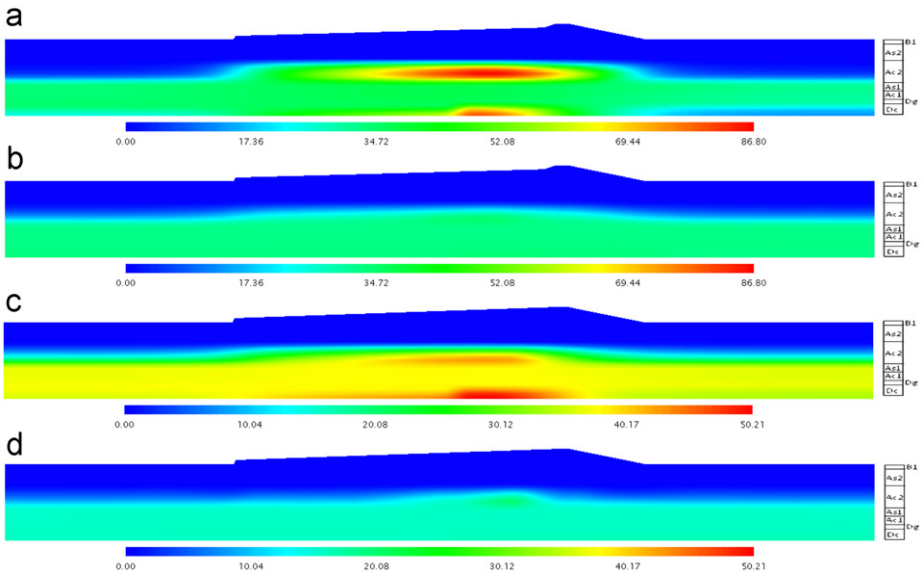

Fig. 20. Excess pore water pressure contours for Case N1 at various steps: (a) 9 months, (b) 22 months, (c) 27 months (EOC), and (d) 10 years after EOC (legend unit: kPa).

6.4. Accumulated viscoplastic shear strain

The accumulated viscoplastic shear strain is obtained by the viscoplastic deviatoric strain increment as $\gamma^{vp} = \int \sqrt{de_{ij}^{vp} de_{ij}^{vp}}$. The accumulated viscoplastic shear strain is an indicator of the deterioration of the materials. The accumulated viscoplastic strain is developed only in clay layers since the elasto-viscoplastic constitutive model is assigned for these layers and the elastic behavior is considered for the sand and gravel layers. The accumulated viscoplastic shear strain contours 10 years after EOC are shown in Fig. 19 for all cases. Among the natural ground cases, the accumulated viscoplastic shear strain in Case N1 is distributed in a whole area of the Ac2-L layer beneath the filling zone with a maximum value of about 4%, with no apparent localization, as shown in Fig. 19(a). For Case N2, however, the application of structural degradation parameters leads to evident strain localization with a maximum value of about 11%, as shown in Fig. 19(b). This value increases to about 18% for Case N3, as can be seen in Fig. 19(c), in the same area as for Case N2. For the improved ground case, in general, smaller levels of viscoplastic shear strain develop compared to Case N3, even

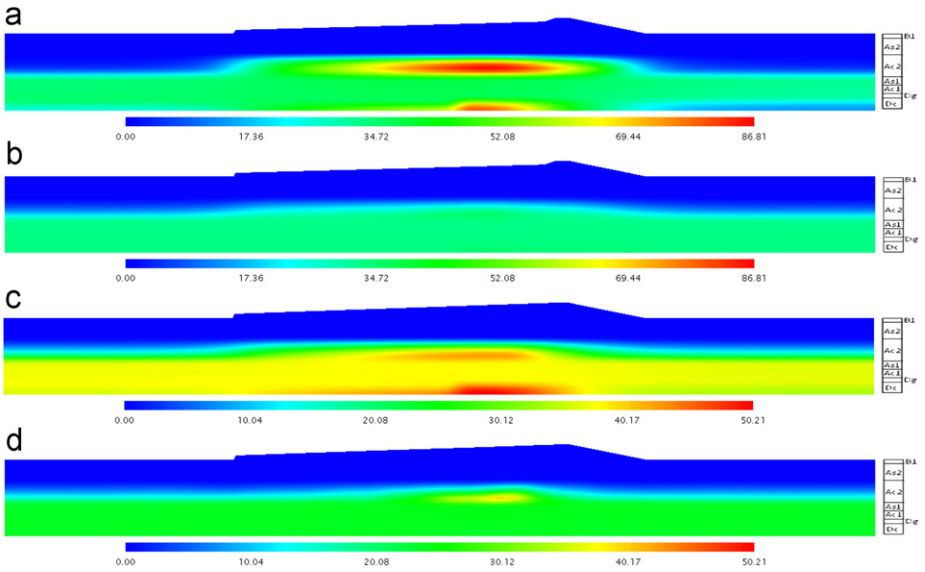

Fig. 21. Excess pore water pressure contours for Case N2 at various steps; (a) 9 months, (b) 22 months, (c) 27 months (EOC), and (d) 10 years after EOC (legend unit: kPa).

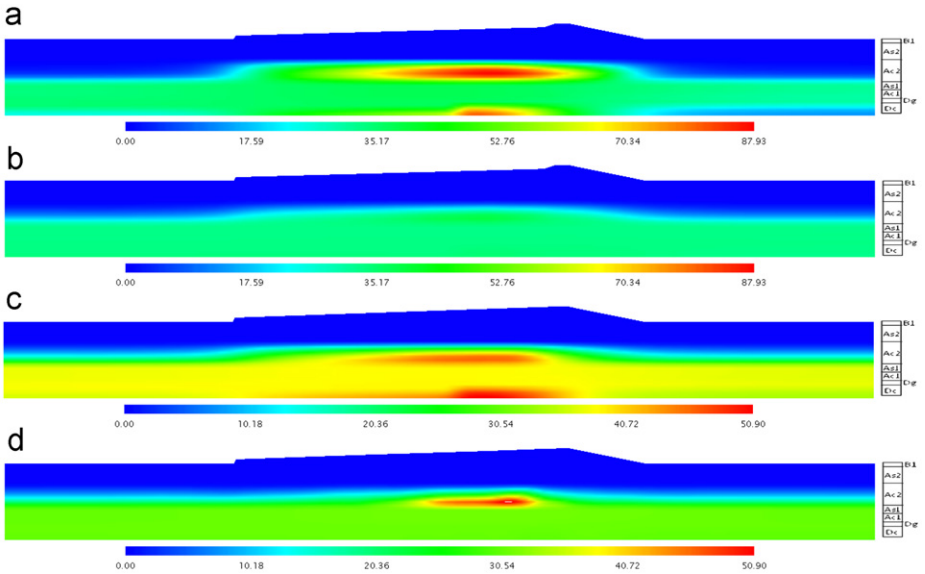

Fig. 22. Excess pore water pressure contours for Case N3 at various steps; (a) 9 months, (b) 22 months, (c) 27 months (EOC), and (d) 10 years after EOC (legend unit: kPa).

though significant strain localization is already observed in layer Ac2 beneath the back slope with a maximum value of about 6%, as illustrated in Fig. 19(d).

6.5. Excess pore water pressure

The excess pore water pressure distribution contours are presented in Figs. 20–23 for natural ground cases N1, N2, and N3 and the improved ground case at various stages of construction. Due to the high permeability of the embankment materials and the upper layers of the ground, the excess pore water pressure mostly develops in the clay layers beneath the super levee. For the natural ground cases, all three cases present rather similar excess pore water pressure variations during the construction period, namely, 27 months. In these cases, the excess pore water pressure is generated with a maximum value of approximately 87 kPa in 9 months, mainly in the Ac2 layer and slightly in the lower clay layer, Ac1, as shown in Figs. 20(a), 21(a), and 22(a). After the short-time consolidation, the excess pore water pressure slowly dissipates to a maximum value of about 50 kPa in 22 months at the deeper layers, as shown in Figs. 20(b), 21(b), and 22(b). Following the construction, excess pore water pressure then builds up to a maximum value of about 50 kPa in 27 months, as illustrated in Figs. 20(c), 21(c), and 22(c). During the long-term

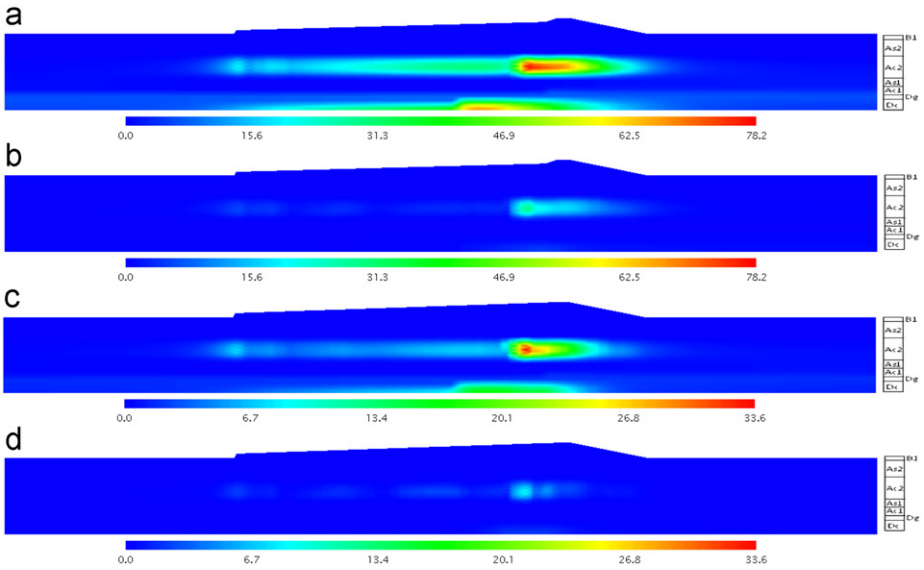

Fig. 23. Excess pore water pressure contours for the improved ground case at various steps: (a) 9 months, (b) 22 months, (c) 27 months (EOC), and (d) 10 years after EOC (legend unit: kPa).

consolidation, however, different responses are observed among the natural ground cases. In Case N1, as shown in Fig. 20(d), after 10 years of consolidation the excess pore water pressure decreases to a value of about 25 kPa, which is widely distributed in layer Ac2 and the layers below it. For Case N2, as shown in Fig. 21(d), giving consideration to the structural degradation of soft clay layers results in the build-up of excess pore pressure after the construction, in the area corresponding to the strain-localized region. The amount of generated excess pore water pressure after the construction in the strain-localized region for Case N3 becomes even higher, since larger structural degradation parameters are assigned. In sensitive soft clay, the pore water pressure increases or becomes stagnant after the completion of the embankment construction, due to the collapse or the rearrangement of the initial clay structure. This anomalous build-up of pore water pressure is associated with the increase in viscoplastic strain and subsequent localization and the high consistency with the strain softening with the decrease in the mean effective stress shown in Fig. 5. This point has been discussed by Kimoto and Oka (2005). The excess pore water pressure in sandy layer As1, between Ac1 and Ac2, is quite a bit higher for the unimproved cases than for the improved case, as shown in Figs. 20–23. This is probably due to the diffusion of the pore water presser developed in clay layer Ac2 and is consistent with the development of viscoplastic volumetric strain shown in Figs. 15–18.

In the improved ground case, the excess pore water pressure distribution is changed by the sand drains and the DM-wall installation. After the first phase of construction in 9 months, as shown in Fig. 23(a), excess pore water pressure is only generated beneath the super levee with a maximum value of about 78 kPa. Due to the sand drain installation, excess pore water pressure is only generated under the embankment construction zone. The presence of sand drains significantly prevents the spreading of the generated pore water pressure to other parts located outside the embankment loading zone. On the other hand, the installation of DM walls under the main levee provides a low-permeability zone over the clay layers, which prolongs the drainage paths and decelerates the dissipation times in that region. During the short-time consolidation, the generated amount is somewhat dissipated and reaches a maximum value of about 30 kPa, as shown in Fig. 23(b). Continuing the construction, this value increases to about 34 kPa, as can be seen in Fig. 23(c), and after 10 years of consolidation, the excess pore water pressure almost dissipates completely, as illustrated in Fig. 23(d). In the improved ground case, as the characteristics of the clay layers have been improved by the pre-loading process, almost no build-up of pore water pressure is observed after the construction of the embankment.

7. Conclusion

The consolidation analysis of a super levee construction project in Torishima, Osaka City, Japan, was conducted using an elasto-viscoplastic constitutive model. As the first phase, the effect of the destructuration of sensitive soft clay, by structural degradation and the strain dependency of the shear modulus, was studied in terms of the consolidation behavior of the super levee construction on a natural (unimproved) ground through three cases. The structural degradation was found to have an excessive effect on the after-construction responses of the pore water pressure and the associated strain localization. On the other hand, the strain dependency of the elastic shear modulus, as another aspect of destructuration in soft clay, was found to affect the behavior at an earlier stage of loading which appears as

relatively large deformations during the construction process, and therefore, during consolidation.

In the second phase of the analysis, the consolidation analysis of the super levee construction was carried out on an improved ground, according to the details of the ground-improvement techniques which have been performed on the site of the project. The field monitored data during the preloading process, prior to super levee construction, was used to obtain the appropriate soil parameters after the improvement. The performance of sand drains, in shortening the drainage paths and accelerating the consolidation rates, was clearly observed through the settlement profiles and the excess pore water pressure contours. The effect of DM walls was observed as reducing the overall settlements beneath the main levee and as creating a low-permeability top layer over the clay layers which decelerates the dissipation rate beneath the main levee. It was found that even after ground improvements, large relative displacements were observed on the ground level and atop the super levee. The predicted large relative settlements atop the super levee in the improved case were found to be consistent with the recent field observed data after the construction (Oka, 2009), in terms of the location and the approximation of the settlement quantities. In addition, the rather large strain localization mainly occurred in the area of the SCP/SD installation, where it is under the highest influence of embankment loading. Consequently, the unevenness of the ground-improvement techniques under the two parts of the super levee, and also the inadequacy of the preloading process in terms of the height/location of temporary fill material and the time of the preloading, can be expressed as the main cause of subsidence in this case even after ground improvements were made. In order to construct a large-scale river embankment for the mitigation of flood disasters, it is necessary to carefully estimate the unequal settlements of ground.

Acknowledgments

This study has been partially supported by the New Technological Development Study Group of the Kinki Regional Development Bureau, Ministry of Land, Infrastructure, Transport and Tourism (MLIT), whose support is acknowledged with thanks and appreciation. In addition, the assistance of the Yodogawa River Office in providing the experimental data is gratefully acknowledged.

References

Adachi, T., Oka, F., 1982. Constitutive equations for normally consolidated clay based on elasto-viscoplasticity. Soils and Foundations 4, 57–70.

Adachi, T., Oka, F., Hirata, T., Hashimoto, T., Nagaya, J., Mimura, M., Pradhan, T.B.S., 1995. Stress–strain and yielding characteristics of eastern Osaka clay. Soils and Foundations 35 (3), 1–13.

Chai, J.C., Shen, S.L., Miura, N., Bergado, D.T., 2001. Simple method of modeling PVD-improved subsoil. Journal of Geotechnical and Geoenvironmental Engineering, ASCE 127 (11), 965–972.

Cheung, Y.K., Lee, P.K.K., Xie, K.H., 1991. Some remarks on two and three dimensional consolidation analysis of sand-drained ground. Journal of Computer and Geotechnics 12, 73–87.

Eringen, C., 2003. Note on Darcy's law. Journal of Applied Physics 94 (2), 1282.

Hardin, B.O., Black, W.L., 1968. Vibration modulus of normally consolidated clay. Proceedings of the ASCE 94 (SM2), 353–369.

Higo, Y., Oka, F., Kodaka, T., Kimoto, S., 2006. Three-dimensional strain localization of water saturated clay and numerical simulation using an elasto-viscoplastic model. Philosophical Magazine 86 (21–22), 3205–3240.

Hird, C.C., Pyrah, I.C., Russell, D., 1992. Finite element modeling of vertical drains beneath embankments on soft ground. Geotechnique 42 (3), 499–511.

Indraratna, B., Redana, I.W., 1997. Plane strain modeling of smear effects associated with vertical drains. Journal of Geotechnical Engineering, ASCE 123 (5), 474–478.

Ishihara, K., 1996. Soil Behavior in Earthquake Geotechnics. Oxford University Press, UK (pp. 85–152).

KG-NET, 2007. Ground of Kansai Area Especially Osaka Plain to Osaka Bay. Kansai Geo-informatics Research Committee, Shin Kansai Jiban (in Japanese).

Kimoto, S., Oka, F., 2005. An elasto-viscoplastic model for clay considering destructuralization and consolidation analysis of unstable behavior. Soils and Foundations 45 (2), 29–42.

Kimoto, S., Oka, F., Higo, Y., 2004. Strain localization analysis of elasto-viscoplastic soil considering structural degradation. Computer Methods in Applied Mechanics and Engineering 193, 2845–2866.

Kimoto, S., Oka, F., Watanabe, T., Sawada, M., 2007. Improvement of the viscoplastic potential and static yield function for the elasto-viscoplastic constitutive model. In: Proceedings of the 62nd Annual Meeting of JSCE, Hiroshima, pp. 637–638 (in Japanese).

Kinki Regional Development Bureau, 2009. Geotechnical Investigation Report of Torishima Super-Levee Project. Osaka, Japan (in Japanese).

Kundzewicz, Z.W., Takeuchi, K., 1999. Flood protection and management: Quo vadimus. Hydrological Sciences Journal 44, 417–432.

Lavallée, J.G., St-Arnaud, G., Gervais, R., Hammamji, Y., 1992. Stability of the Olga C test embankment. In: Seed, R.B., Boulanger, R.W. (Eds.), ASCE Geotechnical Special Publication No. 31, Stability and Performance of Slopes and Embankments II, vol. 2. ASCE, Berkeley, California, pp. 1006–1021.

Matsuo, O., 1996. Damage to river dikes. Soils and Foundations (Special Issue), 235–240.

Mesri, G., Choi, Y.K., 1979, Excess pore water pressure during consolidation. In: Proceedings of the Sixth Asian Regional Conference on SMFE, vol. 1, pp. 151–154.

Mitchell, J.K., 1986. Practical problems from surprising soil behavior, 20th Terzaghi Lecture. Journal of Geotechnical Engineering, ASCE 112 (3), 259–289.

Ogisako, E., Nishio, S., Denda, A., Oka, F., Kimoto, S., 2007. Simulation of triaxial compression tests on soil samples obtained from seabed ground in deep sea by elasto-viscoplastic constitutive equation. In: Chung, Komai (Eds.), Proceedings of the Seventh ISOPE Ocean Mining & Gas Hydrates Symposium. ISOPE, Lisbon, Portugal, pp. 63–68.

Oka, F., 2009. Study on the Deformation Prevention Technology of the Super Levee. Kinki Regional Development Bureau, MLIT, Osaka, Japan (in Japanese).

Oka, F., Higo, Y., Kimoto, S., 2002a. Effect of dilatancy on the strain localization of water-saturated elasto-viscoplastic soil. International Journal of Solids and Structures 39, 3625–3647.

Oka, F., Kodaka, T., Tanaka, K., 2002b. 3-D liquefaction analysis to evaluate the stability of grid-shaped stabilized ground by deep mixing method. In: Proceedings of the 11th Japanese Earthquake Engineering Symposium, pp. 1077–1080 (in Japanese).

Oka, F., Yashima, A., Kohara, I., 1992. A finite element analysis of clay foundation based on finite elasto-viscoplasticity. In: Pande, G.N., Pietruszczak, S. (Eds.), Proceedings of the Fourth International Symposium on Numerical Methods in Geomechanics, vol. 2. Balkema, Swansea, UK, pp. 915–922.

Perzyna, P., 1963. The constitutive equations for work-hardening and rate sensitive plastic materials. Proceedings of the Vibration Problems, Warsaw 4 (3), 281–290.

Potts, D.M., Zdravkovic, L., 1999. Finite Element Analysis in Geotechnical Engineering: Theory. Thomas Telford, UK.

Roscoe, K.H., Schofield, A.N., Thurairajah, A., 1963. Yielding of clays in states wetter than critical. Geotechnique 13 (3), 211–240.

Terzaghi, K., 1944. Ends and means in soil mechanics. Engineering Journal, Canada 27, 608–613.

Uto, K., 1967. Investigation of foundation ground. In: Foundations of Structures. Kanto Branch of Japan Society of Civil Engineers, pp. 33–66 (in Japanese).